ACS Catalysis

pubs.acs.org/acscatalysis

Research Article

Methanol-to-Olefins Catalysis on HSSZ-13 and HSAPO-34 and Its Relationship to Acid Strength

Zhichen Shi, Matthew Neurock,* and Aditya Bhan*

Cite This: *ACS Catal.* 2021, 11, 1222−1232

Read Online

ACCESS | Metrics & More | Article Recommendations | Supporting Information

ABSTRACT: Catalyst lifetime and product selectivity of methanol-to-olefins (MTO) catalysis on isostructural HSSZ-13 and HSAPO-34, possessing Brønsted acid sites of different acid strengths, are examined and interpreted to elucidate the role of acid strength in MTO catalysis with and without high-pressure H_2 co-feeds. MTO catalysis without H_2 cofeeds on HSSZ-13 results in a shorter catalyst lifetime and higher paraffins-to-olefins ratio than on HSAPO-34, plausibly due to faster rates of formaldehyde formation and involvement of formaldehyde in subsequent alkylation reactions that transform active chain carriers to inactive polycyclics on Brønsted acid sites of higher acid strength. Higher reactivities of protons of greater acid strength in catalyzing hydrogenation of hydrocarbons and oxygenates result in a higher increment in lifetime, paraffins selectivity, and methane selectivity on HSSZ-13 than on HSAPO-34 when coprocessing high-pressure H_2 during MTO catalysis as affirmed in independent kinetic studies and density functional theory (DFT) calculations. These results provide mechanistic insights into the critical role of acid strength in influencing catalyst lifetime and product selectivity during MTO catalysis and rationalize, from a mechanistic and kinetic vantage point, why it may be advantageous to use aluminosilicates such as HSSZ-13 in bifunctional catalytic formulations to upgrade syngas mixtures or during MTO catalysis with cofeeds of molecular hydrogen.

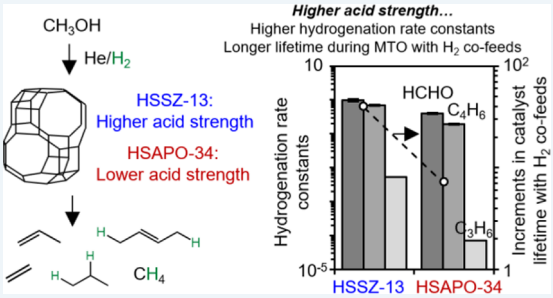

KEYWORDS: *methanol-to-olefins, small-pore zeolites, acid strength, deactivation, hydrogenation kinetics, density functional theory, high-pressure H_2*

1. INTRODUCTION

Methanol-to-olefins (MTO) catalysis on Brønsted acidic zeolites/zeotypes of CHA topology presents a selective route for production of ethylene and propylene (~80%C) because narrow eight-membered windows (3.8 × 3.8 Å) prevent egression of large aliphatics and aromatics that engender the hydrocarbon pool but enable effusion of light olefins.[1−3] The CHA topological features (three-dimensional structure with large ellipsoidal cages, 10 × 6.7 Å, interconnected via narrow eight-membered windows, 3.8 × 3.8 Å) distinguish these window cage-type materials from medium- and large-pore materials where larger channel sizes confer facile elution of aromatics and intercept their involvement in the hydrocarbon pool, which, consequently, requires methanol conversion for "reconstruction" of the hydrocarbon pool and results in lower selectivity toward ethylene and propylene (e.g., <40%C on HZSM-5 with 5.5 Å channel openings[4]). Thus, small pores on window cage-type materials manifest beneficial characteristics for light olefins selectivity; however, they render fast catalyst deactivation that can be tackled by co-feeding high-pressure H_2 during MTO catalysis to scavenge formaldehyde and/or intercept intermediates along dehydrocyclization cascades via their saturation,[5−7] as suggested to be plausible by kinetic studies[5] and density functional theory calculations.[8,9] Arora et al.[5] carried out kinetic studies of hydrogenation reactions on zeolites of varying topologies and attribute the topology-dependent increments in catalyst lifetime and product selectivity during MTO catalysis with H_2 co-feeds to the effects of confinement on hydrogenation reactivities of monoenes and dienes. In addition to solvation by confinement, acid strength is an important property of zeolites and zeotypes that impacts their catalytic function,[10−15] contributing to differences observed in their lifetime and product selectivity during MTO catalysis as demonstrated by Yuen et al.[16] and Bleken et al.[13] These studies, however, do not (i) justify the origins of the observed acid strength-dependent MTO behaviors without H_2 co-feeds, (ii) provide comparisons of these materials during MTO catalysis with high-pressure H_2 co-feeds that resemble conditions of MTO catalysis during syngas-to-olefins conversion,[17−19] (iii) provide experimental evidence for hydrogenation of formaldehyde despite prior

Received: September 12, 2020
Revised: December 23, 2020

https://dx.doi.org/10.1021/acscatal.0c04011
ACS Catal. 2021, 11, 1222−1232

speculations of its viability,[8,9] or (iv) make direct comparisons between experimentally measured and theoretically calculated transition state energies during the hydrogenation of hydrocarbons and oxygenates.

Here, we investigate the methanol-to-olefins on isostructural silicoaluminate and silicoaluminophosphate materials, HSAPO-34 and HSSZ-13, both characterized by the CHA framework type, and interpret the chemical composition-dependent increment in lifetime, paraffins selectivity, and methane selectivity during MTO catalysis with H_2 co-feeds using a combination of kinetic studies and density functional theory calculations. We attribute lower lifetime and olefins-to-paraffins ratio during MTO catalysis on HSSZ-13 than on HSAPO-34 to acid strength-dependent hydrogen transfer rates, quantified by higher formaldehyde selectivity during MTO catalysis on HSSZ-13. We demonstrate that co-feeding high-pressure H_2 during MTO catalysis results in a longer lifetime on HSSZ-13 than on HSAPO-34 with concomitant increments in the paraffins-to-olefins ratio and methane selectivity. Mechanistically, the notable changes in catalyst lifetime and paraffins and methane selectivities are related to higher reactivities of formaldehyde, 1,3-butadiene, propene, and methanol with high-pressure H_2 over Brønsted acid sites of higher acid strength. These results provide essential mechanistic insights into the effect of acid strength on the rates of methanol transfer (de)hydrogenation and the hydrogenation rates of olefins and oxygenates, which, taken together, result in acid strength-dependent catalyst lifetime and product selectivity during MTO catalysis with and without H_2 co-feeds.

2. MATERIALS AND METHODS

2.1. Catalyst Characterization. Structural and chemical characteristics of HSSZ-13 and HSAPO-34 materials used in this study probed using powder X-ray diffraction, N_2 physisorption, scanning electron microscopy, ^{29}Si MAS NMR, and ammonia thermal desorption (TPD) have been reported previously[5,6] and are summarized in Table 1. Both

Table 1. Physical and Chemical Characteristics of Zeolites Used in the Study

	HSSZ-13	HSAPO-34
BET surface area[a] ($m^2\ g^{-1}$)	560	554
micropore volume[a] ($cm^3\ g^{-1}$)	0.28	0.28
H^+ density[b] (mmol g^{-1})	0.44	0.92
Si/Al or (Al + P)/Si[c]	12.9	10.3
deprotonation energy[d] (kJ mol^{-1})	1221.5	1268.5

[a]Obtained from N_2 physisorption at 77 K. [b]Cumulative amount of NH_3 desorbed upon thermal treatment of NH_4^+-exchanged samples at 823 K. [c]Obtained from energy dispersive X-ray spectroscopy (EDS) measurements. [d]Obtained from theoretical calculations detailed in the Supporting Information (section S2).

HSSZ-13 and HSAPO-34 have cubic morphology with an average crystallite size of ~1 μm as shown by the SEM images (Figure S1, Supporting Information). The bulk crystal structure of HSSZ-13 and HSAPO-34 matched the reported structure for CHA,[20] as confirmed by XRD patterns (Figure S2, Supporting Information). The ^{29}Si MAS NMR spectrum (Figure S3, Supporting Information) showed one dominant peak at −92.7 ppm, suggesting that the majority of Si atoms are present as isolated Si (i.e., $Si(OAl)_4$) in HSAPO-34. The total number of Brønsted acid sites, determined by NH_3-desorption (Figure S4, Supporting Information), was used to normalize measured hydrogenation rates.

Differences in the acid strength among these isostructural materials have been examined using various experimental methods including probe molecule infrared spectroscopy[21−26] and NMR,[21] adsorption enthalpies of amines, and neutron diffraction.[23] These experimental analyses gave measures of acid strength that depend on the identity of the probe molecule and the location of protons within the microporous voids[27] and thus have been supplanted by more direct and rigorous assessments of acid strength using theoretical methods to calculate the energy required to remove a proton from the solid acid to an infinite separation from its conjugate anion, which is termed the deprotonation energy (DPE).[28−31] Here, we employ DPE values of protons on HSSZ-13 and HSAPO-34 as assessors of their acid strength where DPE values were calculated using eq 1:

$$\mathrm{DPE} = E_{H^+} + E_{Z^-} - E_{ZH} \quad (1)$$

where E_{H^+}, E_{Z^-}, and E_{ZH} are the electronic energies of the proton, deprotonated zeolite anion, and neutral Brønsted acid, respectively. The cluster models for HSSZ-13 and HSAPO-34 were derived from the optimized crystal structure of HSSZ-13 and HSAPO-34 to contain 51 T-atoms where the protons on all four distinct O atoms surrounding a unique T-site were considered[25,32,33] as detailed in the Supporting Information (section S2). Geometry optimizations were carried out on the neutral and deprotonated clusters with computational details summarized in the Supporting Information (section S2). The averaged DPE values are reported in Table 1 where the lower DPE value of HSSZ-13 (1221.5 kJ mol^{-1}) suggests a higher acid strength of protons on HSSZ-13 than those on HSAPO-34 (1268.5 kJ mol^{-1}). These values are in line with DPE values calculated by Sauer et al.[34,35] using a combined quantum mechanistics−intermolecular potential function approach (QM-Pot).

2.2. Catalytic Testing. All experiments were performed in a tubular glass-lined stainless steel reactor (6.35 mm O.D. and 4 mm I.D., SGE Analytical Science) placed in a resistively heated furnace (Applied Test Systems). The reaction temperature was measured using a K-type thermocouple (Omega) wrapped around the reactor peripherally with the tip placed at the center of the catalyst bed and was regulated with an electronic controller (Watlow). Before each reaction, HSAPO-34 or HSSZ-13 (mesh 60−80) was physically mixed with aggregates of sand (subjected prior to an overnight wash in 2 M HNO_3 solution, followed by DI water rinse until pH ≈ 7, and a final thermal treatment in flowing dry air (1.67 $cm^3\ s^{-1}$) at 1273 K (0.083 K s^{-1} ramp rate from room temperature) for 16 h) with a sand-to-zeolite mass ratio of ~10 and pretreated in flowing dry air (1.67 $cm^3\ s^{-1}$) at 873 K (0.0167 K s^{-1}) for 6 h prior to cooling to the desired reaction temperature in helium flow (1.67 $cm^3\ s^{-1}$). The gas-phase pressure was controlled with a back-pressure regulator (TESCOM Series 44-2300) and measured using pressure transducers (Omega) placed upstream and downstream of the reactor tube. The composition of the reactant and product streams were quantified using a gas chromatograph (Agilent GC 7890A) equipped with a dimethylpolysiloxane HP-1 column (50 m × 320 μm × 0.52 μm) connected to a flame ionization detector for detection of hydrocarbons and oxygenates and a PorapakQ column (4.6 m × 3.2 mm × 2 mm) connected to a thermal

https://dx.doi.org/10.1021/acscatal.0c04011
ACS Catal. 2021, 11, 1222−1232

conductivity detector for detecting permanent gases (H_2 and Ar).

Methanol reactions were carried out on HSSZ-13 and HSAPO-34 at 673 K and space velocities of ~1600 mol_C $(mol_{H+}\ ks)^{-1}$ that resulted in subcomplete methanol conversion. Methanol (Chromasolv, Honeywell) was fed using a 100 cm^3 stainless-steel syringe (Harvard apparatus) and PHD ULTRA XF syringe pump (Harvard Apparatus) to heated lines and carried by the gas stream (He (99.9999%, Matheson) or H_2 (99.9999%, Matheson) and internal standard (Ar (99.9999%, Matheson)) whose flow was controlled by mass flow controllers (Brooks 5850E). The conversion was calculated based on the amount of methanol/dimethyl ether (DME)-derived carbon observed in effluent hydrocarbons. The total turnover number was calculated as the total amount of methanol/dimethyl ether-derived carbon atoms observed in the products normalized by the number of Brønsted acid sites in the catalyst bed when the conversion drops below ~15%C.

Hydrogenation reactions were carried out with high-pressure H_2 at varying temperatures (673 K for propene and 1,3-butadiene, 523 K for formaldehyde and methanol) to ensure high selectivity of first hydrogenated analogs during propene, 1,3-butadiene, and formaldehyde hydrogenation—propane (>90%; balance CH_4 and C_2H_4 likely resulting from cracking of C_3H_8 or C_3H_6 oligomers), a mix of butene isomers (>90%; balance C_2H_4 and C3H6 likely resulting from cracking of C_4H_8 or C_4H_8 oligomers), methanol (>99%)—, and methane and DME being the sole products during methanol hydrogenation. Differential conversions were maintained at all reaction conditions (<5% conversion on HSSZ-13 and <1% conversion on HSAPO-34). Specifically, temperatures were lowered during formaldehyde and methanol hydrogenation reactions to minimize byproduct formation and catalyst deactivation. Propene (0.1% in balance Ar, Certified Standard, Gasco), 1,3-butadiene (0.05% balance in He, Certified Standard, Praxair), methanol (100 ppm balance in He, Certified Standard, Matheson), H_2 (99.9999% Matheson), and Ar (99.9999%, Matheson; used as the internal standard) flows were metered using mass-flow controllers (Brooks 5850E). Formaldehyde trimers (1,3,5-trioxane, ≥99.9%, Sigma-Aldrich) were dissolved in toluene (≥99.9%, Sigma-Aldrich) as an anhydrous formaldehyde source. Liquids (water (HPLC grade) and trioxane/toluene solution (9.1 mol % trioxane)) were fed with a glass syringe (SGE 100 μL or 1 mL) and a syringe pump (Cole Parmer 78-0100C) to heated lines and carried by the gas stream. Specifically, water was co-fed (50 Pa, chosen based on the effluent water-to-propene ratio of ~2.5 during MTO catalysis at conversions >10%) during propene and 1,3-butadiene hydrogenation reactions to mimic MTO reaction environments where water is produced via methanol dehydration. Water was not co-fed during formaldehyde hydrogenation because formaldehyde reacts with water at elevated temperatures via its self-disproportionation to form methanol and formic acid and/or cross-disproportionation with formic acid to form methanol, carbon dioxide, and water, complicating the analysis of methanol formation from formaldehyde hydrogenation.[36,37] Water was not co-fed during methanol hydrogenation to methane to avoid complications resulting from hydration reactions of surface methyl species. Steady-state hydrogenation rates were measured by adjusting reactant flow rates to obtain the desired partial pressures of the respective reagents (0.0001−0.0008 bar for propene, 1,3-butadiene, methanol, and formaldehyde and 2−9 bar for H_2). The measured hydrogenation rates were stable with times on stream (section S3 and Figure S8, Supporting Information) and were invariant with space velocity of the hydrocarbon/oxygenate reactant at high reactant flowrate (section S3 and Figure S9, Supporting Information), indicating that measured rates were not affected by deactivation, secondary reactions, or product inhibition and, as such, high space velocity conditions were chosen for the kinetic measurements in this study.

2.3. Density Functional Theory Calculations. First-principle density functional theory calculations were carried out to optimize the HSSZ-13 and HSAPO-34 structures and determine the structures and energies of the reactants, transition states, and products involved in the hydrogenation of propene, 1,3-butadiene, and formaldehyde. All calculations reported herein were carried out using periodic plane-wave density functional theory (DFT) implemented in the Vienna *ab initio* simulation program (VASP). The calculations were initially carried out using the Perdew−Burke−Ernzerhof (PBE) exchange functional[38] with the core electrons described using projector augmented wave (PAW)-based[39,40] pseudopotentials and the valence electrons represented by a plane-wave basis set with an energy cutoff of 600 eV. The dispersive interactions were calculated using the Grimme-type D3 corrections with Becke−Johnson (BJ) damping.[41,42] The self-consistent field calculations and geometric optimizations were converged to 10^{-6} eV and 0.03 eV $Å^{-1}$, respectively.

The structure of HSSZ-13 was constructed from the Accelrys Materials Studio structure library[43−45] with unit cell $Si_{12}O_{24}$ and lattice parameters $a = b = c = 9.421$ Å and $\alpha = \beta = \gamma = 94.200°$. A single Si atom at the windows connecting the cages (Si/Al = 11, similar to the material used in the experimental studies (Table 1)) was substituted by an Al atom to create a Brønsted acid site (section S2 and Figure S5, Supporting Information). The structure of HSAPO-34 (section S2 and Figure S5, Supporting Information) was modified from the structure of HSSZ-13 and optimized with a higher energy cutoff of 800 eV. The HSAPO-34 has lattice parameters of $a = b = c = 9.423$ Å, $\alpha = \gamma = 94.564°$, and $\beta = 94.563°$ where a single P atom was substituted by a Si atom to create a Brønsted acid site, corresponding to a (Al + P)/Si ratio of 11 (similar to the material used in experimental studies (Table 1)). We note the difference between the CHA structure used in this study and that obtained from the Database of Zeolite Structures[20] but state that the adsorption and transition state energies and structures are not sensitive to the unit cell structure and Si/Al ratio used, as discussed in the Supporting Information (section S4 and Figures S19 and S20).

Transition states were first isolated via the climbing image nudged elastic band (CI-NEB)[46] method using 12 images with a force tolerance of 0.3 eV $Å^{-1}$ and further refined using the dimer method[47] and converged to within 0.03 eV $Å^{-1}$. Frequency calculations were carried out on all optimized structures using a fixed displacement method[48] with self-consistent field convergence at 10^{-8} eV where the adsorbates (e.g., propene and H_2) and AlO_4 sites are displaced by 0.015 Å, while all other framework atoms are fixed. Low-frequency modes (<60 cm^{-1}) were replaced with 60 cm^{-1} because of inaccuracies in the estimations of low frequencies.[8,32,48,49] These frequencies were used to determine zero-point vibration energies (ZPVE) and vibrational enthalpies (H_{vib}) for calculations of temperature-corrected enthalpies using the equation summarized in the Supporting Information (section S4).

https://dx.doi.org/10.1021/acscatal.0c04011
ACS Catal. 2021, 11, 1222−1232

The inclusion of D3 dispersion corrections, which typically provides reliably accurate estimations for adsorption and transition state energies for organic systems,[41,42,50] has been shown to overestimate the binding energies and underestimate the reaction barriers when applied to zeolites,[29,51−54] plausibly due to the fact that D3 corrections have not been parameterized for heterogeneous catalytic systems. These errors can be significantly reduced by using meta-hybrid functionals that treat dispersion without parameterization. The M06-L functional,[55] a meta-generalized gradient approximation (meta-GGA) functional, for example, has been shown to predict binding energies of adsorbates in large zeolitic systems comparable to results obtained from much more accurate *ab initio* MP2 calculations.[56−58] We therefore carried out single-point energy calculations on all of the optimized reactants, transition states, and products using the M06-L functional implemented in VASP to provide more accurate estimation of activation energies and, thus, better comparisons with experimental results.

3. RESULTS AND DISCUSSION

3.1. Comparisons between HSAPO-34 and HSSZ-13 during MTO Catalysis. MTO reactivities, evaluated using catalyst lifetime and product selectivity, differ on HSSZ-13 and HSAPO-34 with varying inlet methanol pressures (10−30 kPa), as shown in Figure 1a,b and Figures S21 and S22

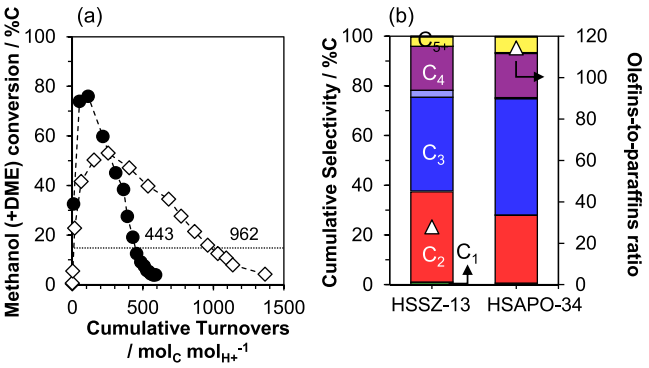

Figure 1. (a) Methanol conversion profiles versus cumulative turnovers; (b) cumulative product selectivity (left ordinate) and the overall olefins-to-paraffins ratio (open triangle, right ordinate) during methanol feeds on HSSZ-13 (solid circle) and HSAPO-34 (open diamond) compared at isoconversion (~15%C, dotted line). Reaction conditions: 673 K; 16 kPa CH_3OH; 1 bar He co-feeds; ~1600 mol$_C$ (mol$_{H+}$ ks)$^{-1}$. The numbers in (a) represent cumulative turnover numbers measured when the conversion dropped below 15%. The dark- and light-shaded bars in (b) represent the olefinic and paraffinic forms, respectively, of the respective carbon group listed in the dark bars.

(section S5, Supporting Information). The catalyst lifetime, as assessed by total turnovers after the conversion drops below 15%, is lower on HSSZ-13 than on HSAPO-34 (~2.0× to 3.0×) at subcomplete methanol conversion with a representative example of conversion profiles shown in Figure 1a where the total turnover is lower on HSSZ-13 by a factor of ~2.2×. This observation is in line with that reported by Bleken et al.[13] and Yuen et al.[16] who carried out similar comparative studies with CHA-type materials of varying acid strength at complete methanol conversion. Recent reports in the literature show that formaldehyde, formed via methanol disproportionation and olefin transfer hydrogenation events, plays an important role in catalyst deactivation by facilitating the transformation of active chain carriers to inactive polycyclic species via electrophilic addition/substitution reactions with olefins and aromatics.[4,59−62] We surmise that the differences in the observed catalyst lifetime on HSSZ-13 and HSAPO-34 reflect acid strength-dependent rates of formaldehyde formation and its involvement in termination sequences.

Figure 2 shows the profiles of formaldehyde and methane selectivities with the number of contact times, times on stream

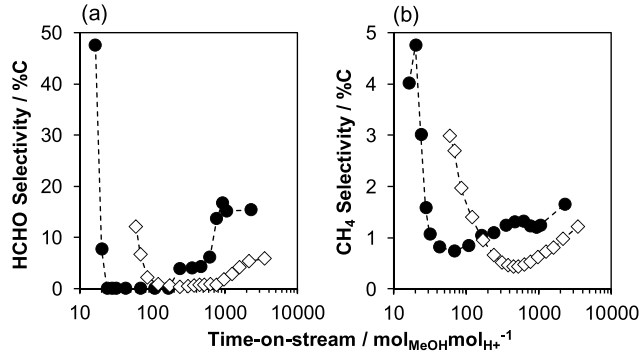

Figure 2. (a) Formaldehyde selectivity and (b) methane selectivity with respect to contact times during methanol feeds on HSSZ-13 (solid circle)and HSAPO-34 (open diamond). Reaction conditions: 673 K; 16 kPa CH_3OH; 1 bar He co-feeds; ~1600 mol$_C$ (mol$_{H+}$ ks)$^{-1}$. Dashed lines are guides for the eye.

scaled by contact time, during MTO catalysis on HSSZ-13 and HSAPO-34. Both formaldehyde and methane selectivities are high at sufficiently early times-on-stream and decrease initially as the reaction progresses with increasing conversion (Figure 2 and Figure S23a), providing direct evidence that formaldehyde and methane are primary products from methanol disproportionation events during methanol-to-hydrocarbon catalysis on proton-form zeolites. This observation is consistent with the transient evolution of methane selectivity reported by Hwang et al.[62] where methane selectivity is high at initial times during MTO catalysis on HSAPO-34. These selectivities eventually increase at later times-on-stream as the catalyst deactivates when relative rates of methanol consumption by the organic cocatalysts decrease in comparison to those for methanol disproportionation events (Figure 2). Higher formaldehyde selectivity on HSSZ-13, when compared at similar conversions (Figure S23a) with that on HSAPO-34, suggests that the net rate of formaldehyde formation via methanol disproportionation events is higher on HSSZ-13, resulting in higher concentrations of formaldehyde. In addition, the formaldehyde selectivity decreases with faster rate of decrements on HSSZ-13 as the reaction progresses, as reflected by a more negative ordinate value in Figure S23b, where the time-on-stream derivative of formaldehyde selectivity is plotted against time-on-stream during MTO catalysis, evidencing faster rates for molecular events prescribing formaldehyde consumption, likely via formaldehyde-mediated alkylation pathways on HSSZ-13. Taken together, faster rates of formaldehyde formation and the rates that describe its involvement in the transformation of active organic cocatalysts to inactive polycyclic species on protons of higher acid strength provide a mechanistic interpretation for a shorter lifetime of HSSZ-13 observed during MTO catalysis. Formation of hydrogen-deficient formaldehyde and aromatics requires the formation of

https://dx.doi.org/10.1021/acscatal.0c04011
ACS Catal. 2021, 11, 1222−1232

hydrogen-rich paraffins in a stoichiometric amount, thus resulting in enhanced formation of paraffins, which manifest in the lower instantaneous and cumulative olefins-to-paraffins ratios on HSSZ-13, as shown in Figure S24 and Figure 1b, respectively.

Co-feeding high-pressure H_2 during MTO catalysis results in an increment in catalyst lifetime on both HSSZ-13 and HSAPO-34 when compared at all conversions below 40% (Figure 3a, section S8, and Figure S25, Supporting

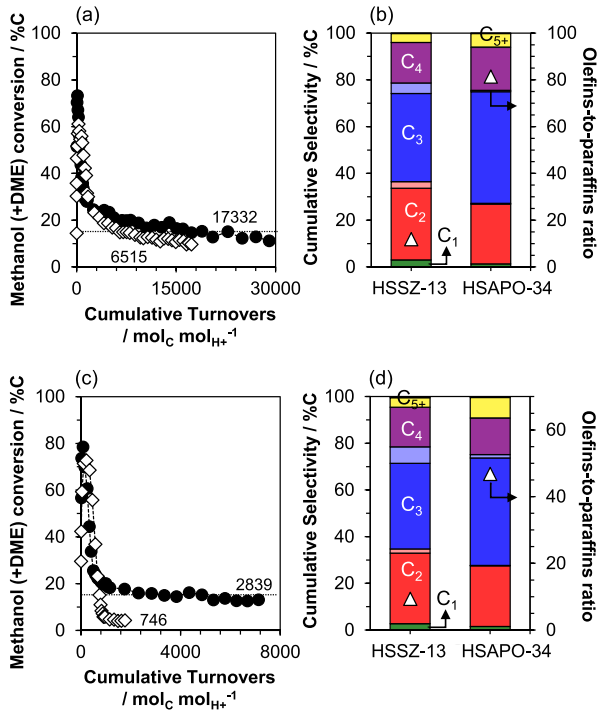

Figure 3. (a, c) Methanol conversion profiles versus cumulative turnovers; (b,d) cumulative product selectivity (left ordinate) and the overall olefins-to-paraffins ratio (open triangle, right ordinate) during methanol feeds on HSSZ-13 (solid circle) and HSAPO-34 (open diamond) compared at isoconversion (~15%C, dotted line). Reaction conditions: 673 K; 16 bar H_2 co-feeds; ~1600 mol_C (mol_{H+} ks)$^{-1}$; 16 kPa (a, b) or 24 kPa (c, d) CH_3OH. The numbers in (a) and (c) represent cumulative turnover numbers measured when the conversion dropped below 15%. The dark- and light-shaded bars represent the olefinic and paraffinic forms, respectively, of the respective carbon group listed in the dark bars.

Information), consistent with reports by Arora et al.[5,6] and Zhao et al.[7] Specifically, such higher increment ratio on HSSZ-13 (~39×) than that on HSAPO-34 (~7×), when compared after the conversion drops below 15%, results in a higher total turnover number of HSSZ-13 in comparison to that on HSAPO-34 with H_2 co-feeds (~2.6×), opposite to the relative lifetime observed during MTO catalysis with He co-feeds where the total turnover number is higher on HSAPO-34 than on HSSZ-13 by a factor of ~2.2× (Figure 1a). Such differences between the lifetimes of HSSZ-13 and HSAPO-34 further increase during methanol conversion with higher inlet methanol pressure (24 kPa) where the total turnover number of HSSZ-13 is higher than that on HSAPO-34 by a factor of ~3.8× (Figure 3c) despite the lifetimes of both HSSZ-13 and HSAPO-34 decreasing due to enhanced rates of methanol dehydrogenation and active chain carrier termination with increasing methanol pressure.[62] We attribute the higher increments in the lifetime of HSSZ-13 during MTO catalysis with high-pressure H_2 co-feeds to the higher reactivities of formaldehyde and/or intermediates along formaldehyde-mediated alkylation pathways (e.g., 1,3-butadiene) with H_2 on protons of higher acid strength as evidenced by kinetic studies detailed in Section 3.2 and theoretical calculations detailed in Section 3.3. The higher reactivities of these deactivation precursors with high-pressure H_2 compensate for higher rates of formaldehyde formation on protons of higher acid strength to result in smaller increments in the net formation of formaldehyde with increasing methanol pressure and, consequently, a smaller decrement or longer lifetime on HSSZ-13 than that on HSAPO-34 during MTO catalysis with elevated inlet methanol pressure in the presence of high-pressure H_2.

The increments in catalyst lifetime observed are accompanied by changes in product selectivity as shown in Figure 3b,d. The paraffins selectivity increases on both HSSZ-13 and HSAPO-34—by a factor of 2.4 and 1.4, respectively—plausibly due to saturation of olefinic species (e.g., propene) during MTO catalysis in the presence of high-pressure H_2 as demonstrated in a previous study.[5] Such differences in paraffins selectivity further increase with increasing methanol pressure (~1.7× to ~4.6× with a methanol inlet pressure from 16 to 24 kPa, Figure 3b,d) as increasing methanol pressure enhances the rates of hydrogen transfer events on HSSZ-13 relative to that on HSAPO-34.[62] We further postulate that the higher increment factor in paraffins selectivity while coprocessing high-pressure H_2 can be related to higher reactivities of these olefinic species with H_2 on protons of higher acid strength. In addition to increments in paraffins selectivity, methane selectivity increases on both HSSZ-13 (Figure 3b, ~2.9×) and HSAPO-34 (Figure 3b, ~1.9×) during MTO catalysis with H_2 co-feeds. The methane selectivity increases further during methanol conversion at a lower temperature with an increment factor of ~14.8× and ~7.7× on HSSZ-13 and HSAPO-34, respectively (reported previously by Arora et al.[5] and summarized in section S9 and Figure S26, Supporting Information). We hypothesize that reduced temperatures decrease rates describing the involvement of methoxyls in methylation reactions with olefins and aromatics relative to hydrogenation rates of methoxyls or hydrogen transfer, resulting in higher methane selectivity observed during MTO catalysis at lower temperatures. Such observations, along with kinetic studies detailed in Section 3.2, suggest that direct hydrogenation of methoxyls to methane may contribute to the much higher methane selectivity (~10%C) observed during syngas conversion to olefins where methanol conversion takes place in the presence of high-pressure H_2.[17]

3.2. Hydrogenation Kinetics of Propene, 1,3-Butadiene, Formaldehyde, and Methanol. In this section, we report the hydrogenation rate constants of propene, 1,3-butadiene, formaldehyde, and methanol with high-pressure H_2 on HSSZ-13 and HSAPO-34 and interpret the effects of acid strength on MTO catalysis in the context of relative reactivities of hydrocarbons and oxygenates with high-pressure H_2. The hydrogenation rates of propene (r_P), 1,3-butadiene (r_B), formaldehyde (r_F), and methanol (r_M), normalized by the total Brønsted acid sites (H^+) in the catalyst bed, were measured under conditions of strict kinetic control and are plotted in Figure 4. The measured hydrogenation rates of propene (r_P), 1,3-butadiene (r_B), and formaldehyde (r_F), normalized by the total Brønsted acid sites (H^+) in the catalyst

https://dx.doi.org/10.1021/acscatal.0c04011
ACS Catal. 2021, 11, 1222−1232

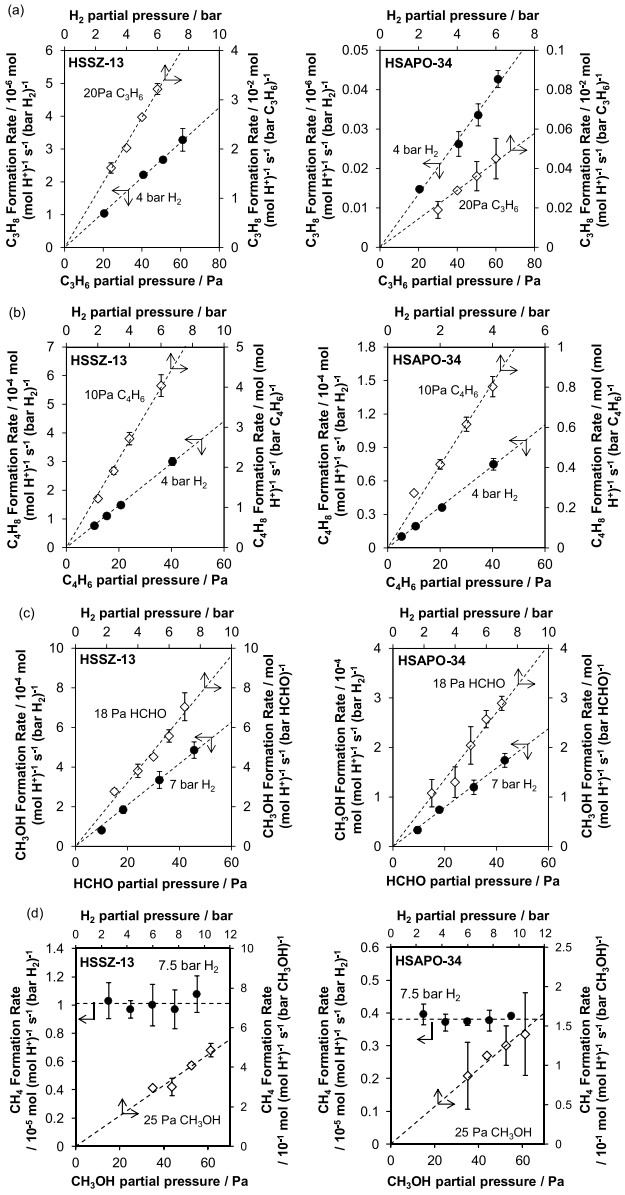

Figure 4. Dependencies of the formation rates of propane, butene, methanol, and methane on partial pressures of the hydrocarbon or oxygenates (solid circle, bottom-left axes) and H_2 (open diamond, top-right axes) during reactions of (a) propene, (b) 1,3-butadiene, (c) formaldehyde, and (d) methanol with H_2 over HSSZ-13 (left) and HSAPO-34 (right) under conditions described in Section 2.2. The vertical bars on each data point represent standard deviations associated with each measurement. The dashed lines represent linear fits to the experimental data. The quantities listed along each line indicate the partial pressure of either the hydrocarbon/oxygenate or H_2 held constant while varying the partial pressure of the other reagent during the kinetic studies.

bed, depend linearly on the partial pressures of hydrocarbons or oxygenates (first-order dependence on partial pressures of propene (P_P), butadiene (P_B), or formaldehyde (P_F)) and H_2 (first-order dependence on partial pressure of hydrogen, P_{H2}) as shown in Figures 4a,c, resulting in overall second-order hydrogenation rate constants for propene (k_P), 1,3-butadiene (k_B), and formaldehyde (k_F) hydrogenation. These relationships can be described by the following equation:

$$\frac{r_{P,B,F}}{[H^+]} = k_{P,B,F}P_{P,B,F}P_{H2} \quad (2)$$

where the k_P, k_B, and k_F are generic representations of overall second-order hydrogenation rate constants for propene, 1,3-butadiene, and formaldehyde hydrogenation, respectively. The normalized hydrogenation rates of methanol depend linearly on the partial pressure of H_2 but remain invariant with methanol partial pressure. Such a relationship can be described by a rate expression shown in eq 3 where k_M represents an overall first-order hydrogenation rate constant describing methanol hydrogenation:

$$\frac{r_M}{[H^+]} = k_M P_{H2} \quad (3)$$

The observed propane and butene formation rate dependencies are consistent with those reported by Arora et al.[5] where the rate expression (eq 2) can be rationalized with a set of elementary steps with the hydrogenation of alkyl intermediates by intrazeolite H_2 species being the sole rate-determining step and Brønsted acid sites being the most abundant surface species (MASI). The dependence of the formation rates of methanol and methane from formaldehyde and methanol, respectively, can be rationalized by a similar set of elementary steps where the sole rate-limiting step is the hydrogenation of the oxocarbenium ion and of the methoxyl group, respectively. The linear dependencies of the measured rates with respect to formaldehyde partial pressure suggest that Brønsted acid sites remain as the sole MASI during the hydrogenation of formaldehyde. In contrast, the zeroth-order dependence of the measured methane formation rates with respect to methanol partial pressure suggests that surface methoxyls or methanol monomers/dimers are the most abundant reactive intermediates under experimental conditions, as detailed in the Supporting Information (section S10) and suggested to be plausible during methanol dehydration kinetics on CHA under similar reaction conditions.[12,27,33]

The second-order hydrogenation rate constants of propene (k_P), 1,3-butadiene (k_B), and formaldehyde (k_F) and the first-order hydrogenation rate constants of methanol (k_M) on HSSZ-13 and HSAPO-34 can be calculated from the slope of the linear fits to the observed rate measurements and are summarized in Table 2.

As shown in Table 2, the hydrogenation rate constants of 1,3-butadiene are at least two orders of magnitude higher than the corresponding values for propene on HSSZ-13 and HSAPO-34, consistent with prior measurements on zeolites of varying topologies.[5] In addition, the hydrogenation rate constants of formaldehyde, a diene precursor, are higher than

Table 2. Measured Second-Order Hydrogenation Rate Constants [mol (mol H^+)$^{-1}$ s^{-1} (bar R)$^{-1}$ (bar H_2)$^{-1}$] of Propene (k_P), 1,3-Butadiene (k_B), and Formaldehyde (k_F) and First-Order Hydrogenation Rate Constants [mol (mol H^+)$^{-1}$ s^{-1} (bar H_2)$^{-1}$] of Methanol (k_M) with H_2 over HSSZ-13 and HSAPO-34 at 673 K (k_P and k_B) and 523 K (k_F and k_M) and their Standard Deviations

	HSSZ-13	HSAPO-34
k_P	$5.31 \times 10^{-3} \pm 8.45 \times 10^{-5}$	$7.00 \times 10^{-5} \pm 2.44 \times 10^{-5}$
k_B	$7.00 \times 10^{-1} \pm 5.95 \times 10^{-2}$	$2.36 \times 10^{-1} \pm 8.54 \times 10^{-2}$
k_F	$9.78 \times 10^{-1} \pm 8.71 \times 10^{-2}$	$3.95 \times 10^{-1} \pm 3.43 \times 10^{-2}$
k_M	$1.07 \times 10^{-5} \pm 1.80 \times 10^{-6}$	$3.67 \times 10^{-6} \pm 2.28 \times 10^{-6}$

https://dx.doi.org/10.1021/acscatal.0c04011
ACS Catal. 2021, 11, 1222−1232

those of 1,3-butadiene (~1.4× on HSSZ-13 and ~1.7× on HSAPO-34) despite rates of formaldehyde hydrogenation being measured at lower temperatures (523 K vs 673 K). The relative hydrogenation reactivities of formaldehyde, diene, and monoene are corroborated by theoretical calculations, which predict (i) significantly lower transition state energies for formaldehyde hydrogenation versus ethene hydrogenation as a result of the proton affinity differences between C=O and C=C,[9] (ii) lower energies of allylic carbocations, intermediates involved in diene hydrogenation, in comparison to the energies of alkycarbenium ions, intermediates involved in monoene hydrogenation,[8] and (iii) lower transition state energies for formaldehyde hydrogenation than that for diene hydrogenation on HSAPO-34 and HSSZ-13.[9] These kinetic data and theoretical calculations suggest that high-pressure H_2 renders both C=O and C=C hydrogenation kinetically accessible to suppress formaldehyde-mediated chain carrier termination pathways by hydrogenating formaldehyde to methanol and dienes to monoenes. The higher hydrogenation rate constants of formaldehyde and 1,3-butadiene on HSSZ-13 than on HSAPO-34—by a factor of 3.6 and 2.4, respectively—suggest higher reactivities of deactivation precursors with H_2 on protons of higher acid strength outpaces higher rates of formaldehyde formation on protons of higher acid strength to result in higher increments in the lifetime of HSSZ-13 during MTO catalysis with H_2 cofeeds (Figures 3 and 5). These

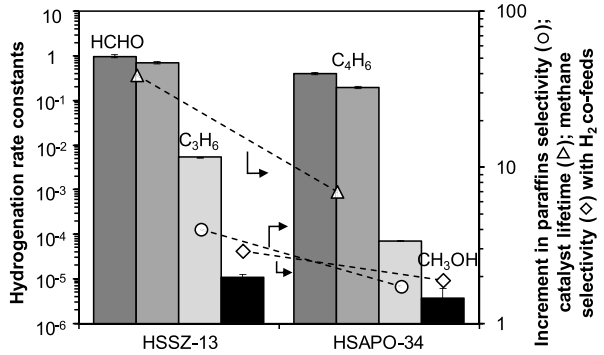

Figure 5. Measured second-order hydrogenation rate constants [mol (mol H^+)$^{-1}$ s^{-1} (bar R)$^{-1}$ (bar H_2)$^{-1}$] of propene (C_3H_6), 1,3-butadiene (C_4H_6), and formaldehyde (HCHO) and first-order hydrogenation rate constants [mol (mol H^+)$^{-1}$ s^{-1} (bar H_2)$^{-1}$] of methanol (CH_3OH) on HSSZ-13 and HSAPO-34 (left, bars) and the increments in paraffins selectivity (right, open circle), catalyst lifetime (right, open triangle), and methane selectivity (right, open diamond) during MTO catalysis on HSSZ-13 and HSAPO-34 with high-pressure H_2 co-feeds. Reaction conditions are listed in Section 2.2.

results suggest that protons of higher acid strength manifest advantageously for longer catalyst lifetime during MTO catalysis in the presence of high-pressure H_2 (e.g., during direct conversion of syngas to olefins).

The Brønsted acid sites in both HSSZ-13 and HSAPO-34 not only catalyze formaldehyde and diene hydrogenation but also catalyze hydrogenation of monoenes and methoxyls to their saturated analogs as quantified in the hydrogenation kinetic studies of propene and methanol (Table 2), contributing to increments in paraffins (~2.4× on HSSZ-13 and ~1.4× on HSAPO-34) and methane selectivities (~2.9× on HSSZ-13 and ~1.9× on HSAPO-34) during MTO catalysis with high-pressure H_2 co-feeds (Figure 3). The higher hydrogenation rate constants of propene and methanol on HSSZ-13 than on HSAPO-34—by a factor of ~76× and ~5.4×, respectively—suggest that protons of higher acid strength enhance the hydrogenation rates of olefins and methoxyls, resulting in higher increments in paraffins and methane selectivities on HSSZ-13 (Figure 5). Nevertheless, these hydrogenation rate constants are at least two orders of magnitude lower compared to hydrogenation rate constants for formaldehyde and 1,3-butadiene on both HSSZ-13 and HSAPO-34 (Figure 5), and consequently, lifetime enhancements are achieved during MTO catalysis in the presence of high-pressure H_2 while maintain a high overall olefins selectivity (~90%C) (Figure 3).

3.3. Computational Assessment of the Effects of Acid Strength on Hydrogenation Reactivities. The adsorption energies and transition state energies for propene, 1,3-butadiene, and formaldehyde hydrogenation to propane, 2-butene, and methanol, respectively, are calculated using density functional theory (computational details in section S4, Supporting Information) to rationalize the effect of reactant identity and acid strength on the hydrogenation reactivities of hydrocarbons and oxygenates as we discuss below. The electronic energies and enthalpies of reactants, transition states, and products involving all oxygens surrounding the unique T-site were calculated at 0 K and corrected to the temperatures relevant to experimental conditions (673 K for propene and 1,3-butadiene hydrogenation and 523 K for formaldehyde hydrogenation) using the PBE-D3 functional with results summarized in the Supporting Information (section S4). Hydrogenation reactions, irrespective of reactant identity, oxygen sites, or chemical composition, proceed by a concerted proton transfer from zeolite to the π-bond of the reactant (C=C for propene and butadiene and C=O for formaldehyde) and insertion of a H_2 molecule between the π-bonded reactant and the negatively charged zeolitic oxygen as shown in the transition state structures in Figure 6 and Figures S10−S12. The H_2 molecule remains intact in the transition state but is polarized with $H^{\delta-}$ interacting with the π-bond of the reactant and $H^{\delta+}$ interacting with the negatively charged zeolitic oxygen site. The direct deprotonation of the zeolite in the transition state highlights the importance of acid strength in hydrogenation kinetics.

Figure S15 shows that the apparent activation barriers are the lowest for formaldehyde hydrogenation and the highest for propene hydrogenation on both HSSZ-13 and HSAPO-34, as oxocarbenium ion-like intermediates involved in formaldehyde hydrogenation are preferentially stabilized over propoxy groups. In addition, these trends in the relative magnitudes of transition state energies correlate with the relative magnitude of the measured hydrogenation rate constants (Table 2 and Figure 5). Specifically, (i) the lowest transition state energies of formaldehyde hydrogenation are consistent with the highest rate constants of formaldehyde hydrogenation despite the fact that the experimental measurements were carried out at a lower temperature (523 K vs 673 K), and (ii) the higher transition state energies of propene hydrogenation in comparison to those of 1,3-butadiene and formaldehyde hydrogenation are congruent with propene hydrogenation rate constants being at least two orders of magnitudes lower than those measured for formaldehyde and 1,3-butadiene. Further comparisons between HSSZ-13 and HSAPO-34 show that the predicted energy barriers are consistently lower (10−15 kJ mol^{-1}) on HSSZ-13 than on HSAPO-34 for all alkenes and for formaldehyde, consistent with (i) higher hydrogenation rate

https://dx.doi.org/10.1021/acscatal.0c04011
ACS Catal. 2021, 11, 1222−1232

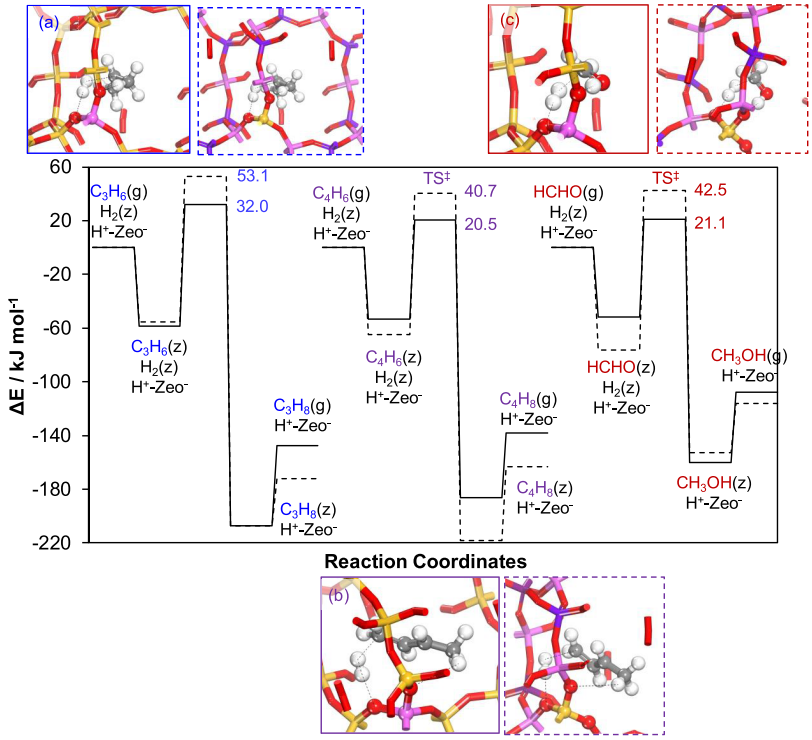

Figure 6. M06-L single-point electronic energies for adsorbed intermediate, transition, and product states calculated relative to the species in the gas phase (C_3H_6 (g), C_4H_6 (g), HCHO (g), and H_2 (g) where g represents the gas phase and z represents the zeolite phase) on HSSZ-13 (solid line) and HSAPO-34 (dashed line) during the hydrogenation of propene to propane (blue), 1,3-butadiene to 2-butene (purple), and formaldehyde to methanol (red). (a), (b), and (c) represent the most stable transition state structures during the hydrogenation of propene, 1,3-butadiene, and formaldehyde, respectively. All of the structures and transition states were initially optimized using the PBE functional with D3 corrections. H atoms (), P atoms (), Al atoms (), Si atoms (), O atoms ().

constants measured on HSSZ-13 than on HSAPO-34 (Table 2 and Figure 5) and (ii) lower activation energy barriers for formaldehyde hydrogenation on HSSZ-13 (~25.8 kJ mol^{-1}) than on HSAPO-34 (~35.8 kJ mol^{-1}) (section S4 and Figure S15, Supporting Information).

The energies calculated using the PBE-D3 functional are comparable with previous DFT results[8,9] but with apparent activation energies much lower than those measured experimentally,[5] with errors greater than 60 kJ mol^{-1} as summarized in Table S4. Similar discrepancies between experiments and DFT predictions using the PBE-D3 functional were obtained for propane dehydrogenation on CHA (section S4, Table S4, and Figure S17, Supporting Information). We attribute such differences to overestimations of binding energies and underestimations of reaction barriers during DFT calculations with the PBE-D3 functional as noted by Goncalves et al.[54] and Hansen et al.[51] As a result, we carried out single-point calculations on PBE-optimized reactants, transition states, and products using the M06-L functional[55] to provide more accurate estimation of adsorption energies and activation energies[56−58] for better comparison with the experimental results. The resultant reaction energy profiles for alkene and oxygenate hydrogenation on HSSZ-13 and HSAPO-34 are shown in Figure 6.

Single-point calculations using M06-L significantly reduce the discrepancies between experimentally measured activation energies and those predicted by DFT calculations from >60 kJ mol^{-1} with PBE-D3 to <15 kJ mol^{-1} as reported in Table S4. These improvements were obtained without changes in the relative activation energy differences for propene, butadiene, and formaldehyde hydrogenation on HSSZ-13 and HSAPO-34 where (i) the activation energies remain lower for formaldehyde and butadiene hydrogenation relative to those for propene hydrogenation, and (ii) the activation energies are higher on HSAPO-34 than on HSSZ-13, consistent with the relative magnitudes of experimentally measured rate constants. We note that the relative trends in the transition state energies for hydrogenation of hydrocarbons and oxygenates were not altered by using either the PBE-D3 functional (Figure S17) or M06-L functional (Figure 6) but propose that higher-level calculations should be considered when comparing experimentally measured activation energies and rate constants with those obtained from DFT calculations.

Taken together, lower activation energy barriers and higher hydrogenation rate constants on HSSZ-13 across hydrocarbons and oxygenates discussed herein suggest higher hydrogenation reactivities on protons of higher acid strength and provide a mechanistic basis for the observed acid strength-dependent catalyst lifetime and product selectivity during MTO catalysis with high-pressure H_2 co-feeds.

4. CONCLUSIONS

The effect of acid strength on methanol-to-olefins catalysis is studied here using isostructural silicoaluminate (HSSZ-13) and silicoaluminophosphate (HSAPO-34). Shorter catalyst lifetime and higher paraffins selectivity were observed during MTO catalysis on HSSZ-13 than on HSAPO-34 as protons of higher acid strength enhance rates describing formaldehyde formation and formaldehyde-mediated alkylation reactions that transform active chain carriers to inactive polycyclic species. Higher

https://dx.doi.org/10.1021/acscatal.0c04011
ACS Catal. 2021, 11, 1222−1232

hydrogenation rate constants of propene, 1,3-butadiene, formaldehyde, and methanol on HSSZ-13, taken together with their lower activation energies calculated using density functional theory, rationalize higher increments in catalyst lifetime and paraffins selectivity on HSSZ-13 than those on HSAPO-34 during MTO catalysis with high-pressure H_2 co-feeds. These results demonstrate the critical effect of acid strength in determining catalyst lifetime and product selectivity during MTO catalysis where catalysts with protons of higher acid strength, although manifesting shorter lifetime during MTO catalysis without H_2 co-feeds, maximize their lifetime during MTO catalysis in the presence of high-pressure H_2.

■ ASSOCIATED CONTENT

Supporting Information

The Supporting Information is available free of charge at https://pubs.acs.org/doi/10.1021/acscatal.0c04011.

Materials characterization; density functional theory calculations; methanol conversion profiles; product selectivity profiles (PDF)

■ AUTHOR INFORMATION

Corresponding Authors

Matthew Neurock − *Department of Chemical Engineering and Materials Science, University of Minnesota, Minneapolis, Minnesota 55455, United States*; Email: mneurock@umn.edu

Aditya Bhan − *Department of Chemical Engineering and Materials Science, University of Minnesota, Minneapolis, Minnesota 55455, United States*; orcid.org/0000-0002-6069-7626; Email: abhan@umn.edu

Author

Zhichen Shi − *Department of Chemical Engineering and Materials Science, University of Minnesota, Minneapolis, Minnesota 55455, United States*

Complete contact information is available at: https://pubs.acs.org/10.1021/acscatal.0c04011

Notes

The authors declare no competing financial interest.

■ ACKNOWLEDGMENTS

We acknowledge financial support from the National Science Foundation (CBET 1701534) and Dow through the University Partnership Initiative. We also acknowledge computational resources from the Minnesota Supercomputing Institute. We thank Dr. Sukaran Arora, Dr. Thomas Chen, Dr. Pragya Verma, Mr. Vineet Maliekkal, and Mr. Ziwei Wang for helpful technical discussions.

■ REFERENCES

(1) Chen, J. Q.; Bozzano, A.; Glover, B.; Fuglerud, T.; Kvisle, S. Recent Advancements in Ethylene and Propylene Production Using the UOP/Hydro MTO Process. *Catal. Today* **2005**, *106*, 103−107.

(2) Yang, M.; Fan, D.; Wei, Y.; Tian, P.; Liu, Z. Recent Progress in Methanol-to-Olefins (MTO) Catalysts. *Adv. Mater.* **2019**, *31*, 1−15.

(3) Tian, P.; Wei, Y.; Ye, M.; Liu, Z. Methanol to Olefins (MTO): From Fundamentals to Commercialization. *ACS Catal.* **2015**, *5*, 1922−1938.

(4) Arora, S. S.; Bhan, A. The Critical Role of Methanol Pressure in Controlling Its Transfer Dehydrogenation and the Corresponding Effect on Propylene-to-Ethylene Ratio during Methanol-to-Hydrocarbons Catalysis on H-ZSM-5. *J. Catal.* **2017**, *356*, 300−306.

(5) Arora, S. S.; Shi, Z.; Bhan, A. Mechanistic Basis for Effects of High-Pressure H_2Co Feeds on Methanol-to-Hydrocarbons Catalysis over Zeolites. *ACS Catal.* **2019**, *9*, 6407−6414.

(6) Arora, S. S.; Nieskens, D. L. S.; Malek, A.; Bhan, A. Lifetime Improvement in Methanol-to-Olefins Catalysis over Chabazite Materials by High-Pressure H_2 Co-Feeds. *Nat. Catal.* **2018**, *1*, 666−672.

(7) Zhao, X.; Li, J.; Tian, P.; Wang, L.; Li, X.; Lin, S.; Guo, X.; Liu, Z. Achieving a Superlong Lifetime in the Zeolite-Catalyzed MTO Reaction under High Pressure: Synergistic Effect of Hydrogen and Water. *ACS Catal.* **2019**, *9*, 3017−3025.

(8) DeLuca, M.; Janes, C.; Hibbitts, D. Contrasting Arene, Alkene, Diene, and Formaldehyde Hydrogenation in H-ZSM-5, H-SSZ-13, and H-SAPO-34 Frameworks during MTO. *ACS Catal.* **2020**, *10*, 4593−4607.

(9) Senger, S.; Radom, L. Zeolites as Transition-Metal-Free Hydrogenation Catalysts : A Theoretical Mechanistic Study. *J. Am. Chem. Soc.* **2000**, *122*, 2613−2620.

(10) Westgård Erichesen, M.; De Wispelaere, K.; Hemelsoet, K.; Moors, S. L. C.; Deconinck, T.; Waroquier, M.; Svelle, S.; Van Speybroeck, V.; Olsbye, U. How Zeolitic Acid Strength and Composition Alter the Reactivity of Alkenes and Aromatics towards Methanol. *J. Catal.* **2015**, *328*, 186−196.

(11) Westgård Erichsen, M.; Svelle, S.; Olsbye, U. The Influence of Catalyst Acid Strength on the Methanol to Hydrocarbons (MTH) Reaction. *Catal. Today* **2013**, *215*, 216−223.

(12) Carr, R. T.; Neurock, M.; Iglesia, E. Catalytic Consequences of Acid Strength in the Conversion of Methanol to Dimethyl Ether. *J. Catal.* **2011**, *278*, 78−93.

(13) Bleken, F.; Bjørgen, M.; Palumbo, L.; Bordiga, S.; Svelle, S.; Lillerud, K.-P.; Olsbye, U. The Effect of Acid Strength on the Conversion of Methanol to Olefins Over Acidic Microporous Catalysts with the CHA Topology. *Top. Catal.* **2009**, *52*, 218−228.

(14) Westgård Erichsen, M.; Svelle, S.; Olsbye, U. H-SAPO-5 as Methanol-to-Olefins (MTO) Model Catalyst: Towards Elucidating the Effects of Acid Strength. *J. Catal.* **2013**, *298*, 94−101.

(15) Chu, Y.; Han, B.; Zheng, A.; Deng, F. Influence of Acid Strength and Confinement Effect on the Ethylene Dimerization Reaction over Solid Acid Catalysts : A Theoretical Calculation Study. *J. Phys. Chem. C* **2012**, *116*, 12687−12695.

(16) Yuen, L.-T.; Zones, S. I.; Harris, T. V.; Gallegos, E. J.; Auroux, A. Product Selectivity in Methanol to Hydrocarbon Conversion for Isostructural Compositions of AFI and CHA Molecular Sieves. *Microporous Mater.* **1994**, *2*, 105−117.

(17) Cheng, K.; Gu, B.; Liu, X.; Kang, J.; Zhang, Q.; Wang, Y. Direct and Highly Selective Conversion of Synthesis Gas into Lower Olefins: Design of a Bifunctional Catalyst Combining Methanol Synthesis and Carbon-Carbon Coupling. *Angew. Chem., Int. Ed.* **2016**, *55*, 4725−4728.

(18) Nieskens, D. L. S.; Lunn, J. D.; Malek, A. Understanding the Enhanced Lifetime of SAPO-34 in a Direct Syngas-to-Hydrocarbons Process. *ACS Catal.* **2019**, *9*, 691−700.

(19) Cheng, K.; Zhou, W.; Kang, J.; He, S.; Shi, S.; Zhang, Q.; Pan, Y.; Wen, W.; Wang, Y. Bifunctional Catalysts for One-Step Conversion of Syngas into Aromatics with Excellent Selectivity and Stability. *Chem* **2017**, *3*, 334−347.

(20) Baerlocher, C.; McCusker, L. *Database of Zeolite Structures* http://www.iza-structure.org/databases/(accessed Aug 23, 2019).

(21) Aufdembrink, B. A.; Dee, D. P.; Mcdaniel, P. L.; Mebrahtu, T.; Slager, T. L. Spectroscopic Characterization of Acidity in Chabazite. *J. Phys. Chem. B* **2003**, *107*, 10025−10031.

(22) Frache, A.; Gianotti, E.; Marchese, L. Spectroscopic Characterisation of Microporous Aluminophosphate Materials with Potential Application in Environmental Catalysis. *Catal. Today* **2003**, *77*, 371−384.

(23) Smith, L. J.; Davidson, A.; Cheetham, A. K. A Neutron Diffraction and Infrared Spectroscopy Study of the Acid Form of the

Aluminosilicate Zeolite, Chabazite (H-SSZ-13). *Catal. Letters* **1997**, *49*, 143−146.
(24) Zecchina, A.; Bordiga, S.; Lamberti, C.; Spoto, G.; Carnelli, L.; Otero Arean, C. Low-Temperature Fourier Transform Infrared Study of the Interaction of CO with Cations in Alkali-Metal Exchanged ZSM-5 Zeolites. *J. Phys. Chem.* **1994**, *98*, 9577−9582.
(25) Bordiga, S.; Regli, L.; Cocina, D.; Lamberti, C.; Bjørgen, M.; Lillerud, K. P. Assessing the Acidity of High Silica Chabazite H - SSZ-13 by FTIR Using CO as Molecular Probe : Comparison with H-SAPO-34. *J. Phys. Chem. B* **2005**, *109*, 2779−2784.
(26) Smith, L.; Cheetham, A. K.; Morris, R. E.; Marchese, L.; Thomas, J. M.; Wright, P. A.; Chen, J. On the Nature of Water Bound to a Solid Acid Catalyst. *Science* **1996**, *271*, 799−802.
(27) Jones, A. J.; Carr, R. T.; Zones, S. I.; Iglesia, E. Acid Strength and Solvation in Catalysis by MFI Zeolites and Effects of the Identity, Concentration and Location of Framework Heteroatoms. *J. Catal.* **2014**, *312*, 58−68.
(28) Maache, M.; Janin, A.; Lavalley, J. C.; Benazzi, E. FT Infrared Study of Brønsted Acidity of H-Mordenites: Heterogeneity and Effect of Dealumination. *Zeolites* **1995**, *15*, 507−516.
(29) Macht, J.; Janik, M. J.; Neurock, M.; Iglesia, E. Mechanistic Consequences of Composition in Acid Catalysis by Polyoxometalate Keggin Clusters. *J. Am. Chem. Soc.* **2008**, *130*, 10369−10379.
(30) Janik, M. J.; Macht, J.; Iglesia, E.; Neurock, M. Correlating Acid Properties and Catalytic Function : A First-Principles Analysis of Alcohol Dehydration Pathways on Polyoxometalates. *J. Phys. Chem. C* **2009**, *113*, 1872−1885.
(31) Brändle, M.; Sauer, J. Acidity Differences between Inorganic Solids Induced by Their Framework Structure . A Combined Quantum Mechanics / Molecular Mechanics Ab Initio Study on Zeolites. *J. Am. Chem. Soc.* **1998**, *120*, 1556−1570.
(32) Deluca, M.; Kravchenko, P.; Hoffman, A.; Hibbitts, D. Mechanism and Kinetics of Methylating C_6-C_{12} Methylbenzenes with Methanol and Dimethyl Ether in H-MFI Zeolites. *ACS Catal.* **2019**, *9*, 6444−6460.
(33) Di Iorio, J. R.; Hoffman, A. J.; Nimlos, C. T.; Nystrom, S.; Hibbitts, D.; Gounder, R. Mechanistic Origins of the High-Pressure Inhibition of Methanol Dehydration Rates in Small-Pore Acidic Zeolites. *J. Catal.* **2019**, *380*, 161−177.
(34) Sauer, J.; Schröder, K. P.; Termath, V. Comparing the Acidities of Microporous Aluminosilicate and Silico-Aluminophosphate Catalysts: A Combined Quantum Mechanics-Interatomic Potential Function Study. *Collect. Czech. Chem. Commun.* **1998**, *63*, 1394−1408.
(35) Sauer, J.; Sierka, M. Combining Quantum Mechanics and Interatomic Potential Functions inAb Initio Studies of Extended Systems. *J. Comput. Chem.* **2000**, *21*, 1470−1493.
(36) Morooka, S.; Wakai, C.; Matubayasi, N.; Nakahara, M. Hydrothermal Carbon-Carbon Bond Formation and Disproportionations of C1 Aldehydes: Formaldehyde and Formic Acid. *J. Phys. Chem. A* **2005**, *109*, 6610−6619.
(37) Morooka, S.; Matubayasi, N.; Nakahara, M. Kinetic Study on Disproportionations of C_1 Aldehydes in Supercritical Water: Methanol from Formaldehyde and Formic Acid. *J. Phys. Chem. A* **2007**, *111*, 2697−2705.
(38) Perdew, J. P.; Burke, K.; Ernzerhof, M. Generalized Gradient Approximation Made Simple. *Phys. Rev. Lett.* **1996**, *77*, 3865−3868.
(39) Blöchl, P. E.; Först, C. J.; Schimpl, J. Projector Augmented Wave Method: Ab Initio Molecular Dynamics with Full Wave Functions. *Bull. Mater. Sci.* **2003**, *26*, 33−41.
(40) Blöchl, P. E. Projector Augmented-Wave Method. *Phys. Rev. B* **1994**, *50*, 17953−17979.
(41) Grimme, S.; Ehrlich, S.; Goerigk, L. Effect of the Damping Function in Dispersion Corrected Density Functional Theory. *J. Comput. Chem.* **2011**, *32*, 1456−1465.
(42) Grimme, S.; Antony, J.; Ehrlich, S.; Krieg, H. A Consistent and Accurate Ab Initio Parametrization of Density Functional Dispersion Correction (DFT-D) for the 94 Elements H-Pu. *J. Chem. Phys.* **2010**, *132*, 154104.
(43) *Materials Studio (Accelrys Inc.)*, Database of Structures.
(44) Fischer, M. Template Effects on the Pressure-Dependent Behavior of Chabazite-Type Fluoroaluminophosphates: A Computational Approach. *Phys. Chem. Miner.* **2019**, *46*, 385−401.
(45) Lee, J. H.; Kim, E. J.; López-Arbeloa, F.; Hong, S. B.; Camblor, M. A. Microporous Aluminophosphates Synthesized with 1,2,3-Trimethylimidazolium and Fluoride. *Dalton Trans.* **2016**, *45*, 7616−7626.
(46) Henkelman, G.; Uberuaga, B. P.; Jónsson, H. A Climbing Image Nudged Elastic Band Method for Finding Saddle Points and Minimum Energy Paths. *J. Chem. Phys.* **2000**, *113*, 9901.
(47) Henkelman, G.; Jónsson, H. Improved Tangent Estimate in the Nudged Elastic Band Method for Finding Minimum Energy Paths and Saddle Points. *J. Chem. Phys.* **2000**, *113*, 9978−9985.
(48) De Moor, B. A.; Ghysels, A.; Reyniers, M. F.; Van Speybroeck, V.; Waroquier, M.; Marin, G. B. Normal Mode Analysis in Zeolites: Toward an Efficient Calculation of Adsorption Entropies. *J. Chem. Theory Comput.* **2011**, *7*, 1090−1101.
(49) Bollini, P.; Chen, T. T.; Neurock, M.; Bhan, A. Mechanistic Role of Water in HSSZ-13 Catalyzed Methanol-to-Olefins Conversion. *Catal. Sci. Technol.* **2019**, *9*, 4374−4383.
(50) Grimme, S.; Steinmetz, M. Effects of London Dispersion Correction in Density Functional Theory on the Structures of Organic Molecules in the Gas Phase. *Phys.Chem.Chem.Phys.* **2013**, *15*, 16031−16042.
(51) Hansen, N.; Kerber, T.; Sauer, J.; Bell, A. T.; Keil, F. J. Quantum Chemical Modeling of Benzene Ethylation over H-ZSM-5 Approaching Chemical Accuracy : A Hybrid MP2 : DFT Study. *J. Am. Chem. Soc.* **2010**, *132*, 11525−11538.
(52) Chiu, C.; Vayssilov, G. N.; Genest, A.; Borgna, A.; Rösch, N. Predicting Adsorption Enthalpies on Silicalite and HZSM-5 : A Benchmark Study on DFT Strategies Addressing Dispersion Interactions. *J. Comput. Chem.* **2014**, *35*, 809−819.
(53) Fraccarollo, A.; Canti, L.; Marchese, L.; Cossi, M. Accurate Evaluation of the Dispersion Energy in the Simulation of Gas Adsorption into Porous Zeolites. *J. Chem. Theory Comput.* **2017**, *13*, 1756−1768.
(54) Goncalves, T. J.; Plessow, P. N.; Studt, F. On the Accuracy of Density Functional Theory in Zeolite Catalysis. *ChemCatChem* **2019**, *11*, 4368−4376.
(55) Zhao, Y.; Truhlar, D. G. A New Local Density Functional for Main-Group Thermochemistry, Transition Metal Bonding, Thermochemical Kinetics, and Noncovalent Interactions. *J. Chem. Phys.* **2006**, *125*, 194101.
(56) Choomwattana, S.; Maihom, T.; Boekfa, B.; Pantu, P.; Limtrakul, J. Density Functional Theory Study on Catalytic Cracking of n-Hexane on Heteropoly Acid: A Comparison with Acidic Zeolite. *Can. J. Chem. Eng.* **2012**, *90*, 865−872.
(57) Kumsapaya, C.; Bobuatong, K.; Khongpracha, P.; Tantirungrotechai, Y.; Limtrakul, J. Mechanistic Investigation on 1,5- to 2,6-Dimethylnaphthalene Isomerization Catalyzed by Acidic β Zeolite: ONIOM Study with an M06-L Functional. *J. Phys. Chem. C* **2009**, *113*, 16128−16137.
(58) Zhao, Y.; Truhlar, D. G. Construction of a Generalized Gradient Approximation by Restoring the Density-Gradient Expansion and Enforcing a Tight Lieb-Oxford Bound. *J. Chem. Phys.* **2008**, *128*, 184109.
(59) Hwang, A.; Bhan, A. Deactivation of Zeolites and Zeotypes in Methanol-to-Hydrocarbons Catalysis: Mechanisms and Circumvention. *Acc. Chem. Res.* **2019**, *52*, 2647−2656.
(60) Hwang, A.; Bhan, A. Bifunctional Strategy Coupling Y_2O_3-Catalyzed Alkanal Decomposition with Methanol-to-Olefins Catalysis for Enhanced Lifetime. *ACS Catal.* **2017**, *7*, 4417−4422.
(61) Müller, S.; Liu, Y.; Kirchberger, F. M.; Tonigold, M.; Sanchez-sanchez, M.; Lercher, J. A. Hydrogen Transfer Pathways during Zeolite Catalyzed Methanol Conversion to Hydrocarbons. *J. Am. Chem. Soc.* **2016**, *138*, 15994−16003.

https://dx.doi.org/10.1021/acscatal.0c04011
ACS Catal. 2021, 11, 1222−1232

(62) Hwang, A.; Kumar, M.; Rimer, J. D.; Bhan, A. Implications of Methanol Disproportionation on Catalyst Lifetime for Methanol-to-Olefins Conversion by HSSZ-13. *J. Catal.* **2017**, *346*, 154−160.

https://dx.doi.org/10.1021/acscatal.0c04011
ACS Catal. 2021, 11, 1222−1232